



Article

# Multifractal and Entropic Properties of Seismic Noise in the Japanese Islands

Alexey Lyubushin

Institute of Physics of the Earth RAS, Moscow 123242, Russia; lyubushin@yandex.ru

## Abstract

This article examines the behavior of seismic noise fields over the Japanese islands recorded by the F-net seismic network for 1997–2025. This paper uses nonlinear noise statistics: the entropy of the wavelet coefficient distribution, the Donoho–Johnston (DJ) wavelet index, and the multifractal singularity spectrum support width. These parameters were chosen because their changes reflect the complication or simplification of the noise structure. Changes in the structure of seismic noise properties are analyzed in comparison with a sequence of strong earthquakes. Using a model of the intensity of interacting point processes, the effect of the leading of local noise property extrema relative to the seismic event times is estimated. Using the Hilbert–Huang decomposition, the synchronization of the amplitudes of the envelopes of noise property time series for different IMF levels is estimated. A sequence of weighted probability density maps of extreme values of noise properties is analyzed in comparison with the mega-earthquake of 11 March 2011 and the preparation of another possible strong seismic event.

**Keywords:** multifractals; wavelets; entropy; point processes; Hilbert-Huang decomposition; principal component analysis; seismic noise; earthquakes; Japan

## 1. Introduction

This article is devoted to the analysis of seismic noise data recorded in the F-net network of stations on the Japanese islands for 29 years, spanning 1997–2025. During this period, on 11 March 2011, a mega-earthquake with a magnitude of 9.1 occurred in Japan. Processes of preparation for strong seismic events are reflected in changes in the properties of seismic noise. The availability of the F-net seismic network with free access to data, provided by the National Research Institute for Earth Science and Disaster Resilience (NIED), makes it possible to test various hypotheses about how changes in the properties of seismic noise reflect the preparation of a strong seismic event. In works [1–3], it was shown that the processes of earthquake preparation are preceded by changes in the statistical structure of seismic noise, consisting in simplification of noise, namely an increase in entropy and a loss of multifractality. This article is a continuation of work [3] on the study of seismic noise in Japan. The possibility of a catastrophic earthquake in the deep-sea Nankai Trough region south of Tokyo has long been a subject of discussion among Japanese seismologists [4,5]. The Tohoku mega-earthquake of 11 March 2011 revived interest in assessing the likelihood of a repeat mega-earthquake in this area [6–8]. A hypothesis was put forward in [8] that a new mega-earthquake could even exceed the Tohoku event in energy, and its magnitude could reach 10. The emergence of new data makes it possible to assess the possibility of a new strong earthquake. This paper shows that significant changes



Academic Editor: Dimitrios Nikolopoulos

Received: 21 January 2026

Revised: 10 February 2026

Accepted: 11 February 2026

Published: 12 February 2026

**Copyright:** © 2026 by the author.

Licensee MDPI, Basel, Switzerland.

This article is an open access article distributed under the terms and conditions of the [Creative Commons Attribution \(CC BY\) license](https://creativecommons.org/licenses/by/4.0/).

in the spatiotemporal structure of seismic noise in Japan occurred in 2020–2025, which may indicate an acceleration of the preparation processes for a new mega-earthquake.

The sources of energy of low-frequency seismic noise energy mostly have atmospheric origin; the crust is the medium for seismic wave propagation. Thus, preparation of strong seismic events are reflected in changes in the properties of seismic noise. The parameters studied were selected after reviewing a large number of other seismic noise properties because they responded most sensitively to the emergence of areas of increased seismic hazard during retrospective analysis. This experience is reflected in publications [1–3].

This article examines the relationship between local extremum points of three seismic noise properties and the times of seismic events. Seismic noise properties have the form of a conventional time series with a constant time step of 1 day. A sequence of earthquakes has the structure of a point process, that is, a sequence of time points in which the intervals between events have varying durations and can be either short (e.g., for aftershocks following strong events) or long (seismic lulls). To enable correlation of conventional time series with a constant time step with point processes, this article transforms the time series into point processes by taking the times of the most prominent local extremums of the seismic noise properties time series. It should be emphasized that the result of this transformation depends heavily on which local extrema are taken (maxima or minima).

## 2. Initial Data

The analysis was performed using vertical seismic oscillation data with a sampling frequency of 1 Hz [9]. These data are available at the address for 78 seismic stations of the F-net network in Japan (Figure 1). The analysis was performed over the period from the beginning of 1997 to 31 December 2025. Seismic data with a sampling frequency of 1 Hz were normalized to a time step of 1 min by calculating the average values in non-overlapping intervals of 60 time samples.

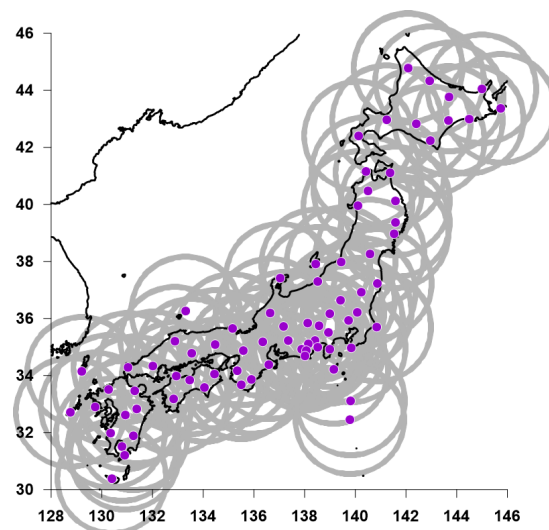


**Figure 1.** Purple dots represent the locations of F-net seismic stations on the Japanese islands. Gray circles are drawn with a radius of 250 km centered on each station. The union of these circles represents the network’s “area of influence,” which is being explored further.

Figure 2 presents the number of working stations each day. A seismic station is considered operational for the current day if there are no gaps during that day. Figure 3 present a sequence of earthquakes with magnitudes not less than 6.

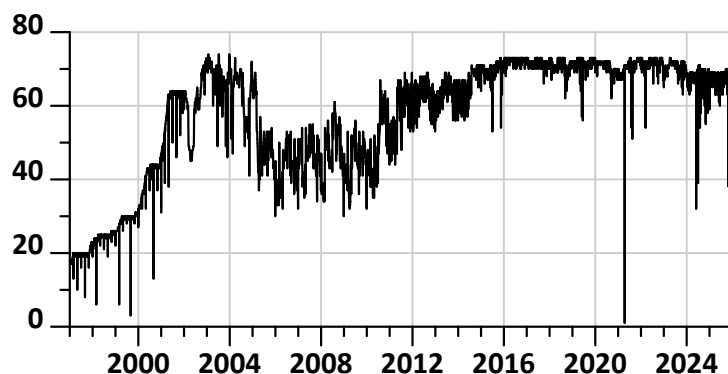


Figure 2. Number of daily operating stations of the F-net network.

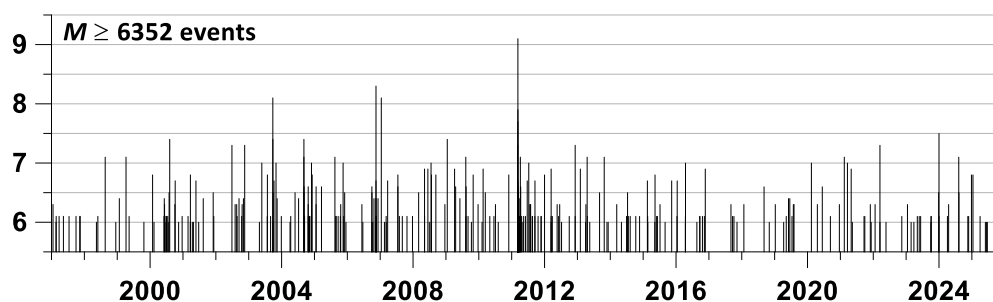


Figure 3. Sequence of 352 seismic events with magnitude  $M \geq 6$  in the region, presented in Figure 1 for the time period 1997–2025. Data source [10].

### 3. Seismic Noise Statistics

The *minimum entropy* of a time series is determined by the formula  $En = -\sum_k p_k \cdot \log(p_k) / \log(N)$ , where  $p_k = c_k^2 / \sum_j c_j^2$ ,  $c_k$  are the wavelet coefficients of the signal decomposition, and  $N$  is the total number of coefficients  $c_k$ . Seventeen orthogonal Daubechies wavelets were used: 10 ordinary minimum support bases with a number of vanishing moments from 1 to 10, and 7 symlets [11] with a number of vanishing moments from 4 to 10. In each time window, the wavelet for which the value  $En$  is minimal is selected.

This set of basis wavelet functions represents a “vocabulary” of bases with a minimum support width and a number of vanishing moments from 1 (Haar wavelet) to 10 [11]. Increasing the number of vanishing moments above 10 is associated with an increase in the calculation error of the basic functions and is usually not used in practice.

The *Donoho–Johnston (DJ) wavelet-based index*  $\gamma$  is the share of “large” wavelet coefficients in absolute value of their total number. By definition,  $0 \leq \gamma \leq 1$ . The threshold separating “large” wavelet coefficients is  $\sigma\sqrt{2 \cdot \ln N}$ , where  $\sigma = \text{med}\left\{\left|c_k^{(1)}\right|, k = 1, \dots, N/2\right\} / 0.6745$  is a robust estimate of the standard deviation of the normal distribution,  $c_k^{(1)}$  are the wavelet coefficients at the first detail level of decomposition, and  $N/2$  is the number of such coefficients [11,12].

The *singularity spectrum support width*  $\Delta\alpha = \alpha_{\max} - \alpha_{\min}$  is considered as a measure of the diversity of the stochastic behavior of the signal. Here,  $\alpha_{\min}$  and  $\alpha_{\max}$  are the minimum and maximum values of the Hölder–Lipschitz exponent [13], which governs the behavior of the signal in the vicinity of the time instant  $t$ :  $|u(t + \frac{\delta}{2}) - u(t - \frac{\delta}{2})| \sim |\delta|^\alpha$ ,  $\delta \rightarrow 0$ . For a monofractal signal, the exponent  $\alpha$  is the same for all time instants  $t$ . If this exponent differs, then the signal is multifractal [14].

After switching to a 1 min sampling time step, the seismic records from each station were divided into 1-day-long time fragments (1440 samples), and the parameters ( $En, \gamma, \Delta\alpha$ )

of daily seismic noise signals were calculated for each fragment. The methods for estimating the parameters  $En$ ,  $\gamma$  and  $\Delta\alpha$  for seismic noise records in a moving time window are presented in [3]. The DFA method [15] was used to calculate the values of the singularity spectrum carrier width. Detrending of seismic noise signals using an 8th-order polynomial was used before calculating the entropy and index in each daily time window. Thus, time series of values with a 1-day time step were obtained for each of the seismic stations. The graphs of these quantities are presented in Figure 4(a1,b1,c1).

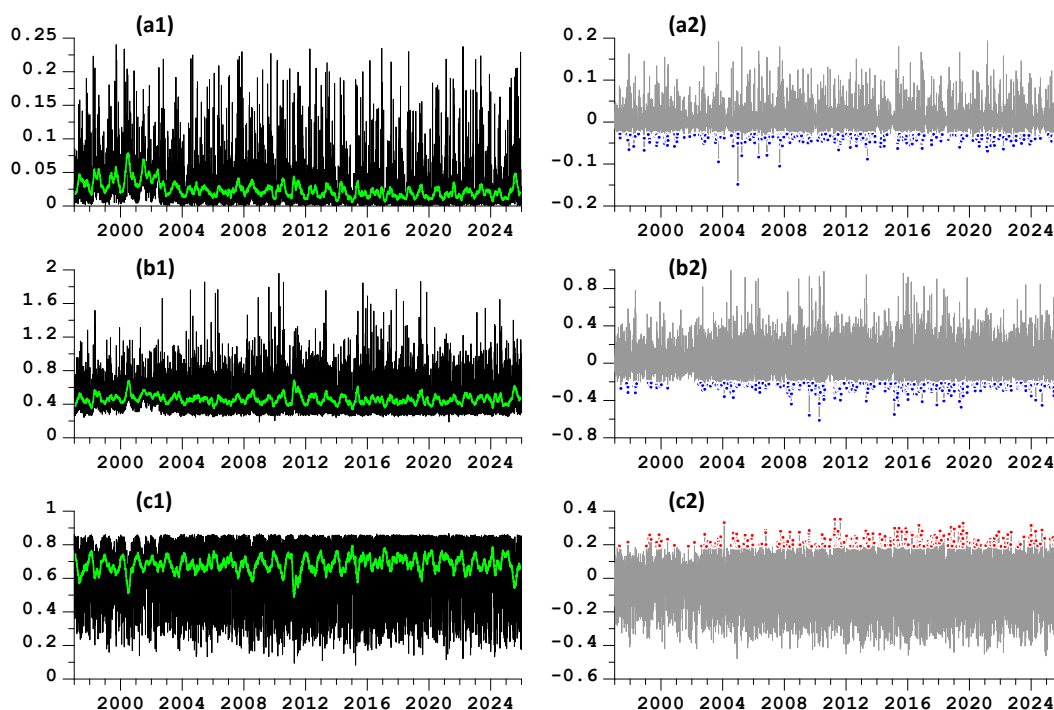


**Figure 4.** Figure (a1,b1,c1) present the graphs of daily median values of  $\gamma$ ,  $\Delta\alpha$  and  $En$ , respectively. The green lines represent the moving averages in a 57-day window. The gray lines in Figure (a2,b2,c2) represent the result of removing local trends with a Gaussian smoothing window of radius 2 days for the curves presented in Figure (a1,b1,c1). The blue dots in Figure (a2,b2) represent the 352 smallest local minima of the values  $\gamma$  and  $\Delta\alpha$  after removing local trends; the red dots in Figure (c2) represent the 352 largest local maxima of the entropy values  $En$  after removing local trends. The number 352 is the number of earthquakes with a magnitude of at least 6 in the rectangular area shown in Figure 1, 1997–2025 (Figure 3).

The question of choosing the best order 8 of the polynomial for trend removal is discussed in detail in [2] and is driven by the need to remove the influence of tidal and thermal trends in low-frequency seismic noise.

The entropy value  $En$  used in this paper, defined through the coefficients of the orthogonal wavelet decomposition, has features in common with multiscale entropy used, for example, in biology [16,17]. In [18,19], entropy is used within the framework of the natural time approach for seismic data analysis. In [20,21], non-extensive Tsallis entropy is used for processing seismic noise data.

The use of multifractal analysis to study the behavior of various complex systems has a long history. Particular attention is paid to the effect of parameter  $\Delta\alpha$  reduction (loss of multifractality) preceding changes in system properties. In medicine, a decrease in the  $\Delta\alpha$  value of various parameters accompanies age-related changes [22–24]. In [25,26], multifractal analysis is used to analyze geoelectric signals and wind speed. Within the framework of the natural time approach, multifractal analysis is used to study both seismicity and other time sequences [27,28].

The purpose of using the seismic noise statistics under study is to identify deviations from the conventional distribution law of their properties (e.g.,  $1/f$ ) that are interpreted as an approximation to the properties of white noise, rather than a complete coincidence with white noise. These deviations are temporary in nature, while the fulfillment of the  $1/f$  law is the result of an assessment over long time intervals. Due to the orthogonality of wavelet basis functions, the total oscillation energy is equal to the sum of the squares of the wavelet coefficients (Parseval equality) [11]. Thus, the wavelet entropy used is, by its construction, the entropy of the oscillation energy distribution over discrete frequency–time “atoms,” each of which is equal to the square of the wavelet coefficients. This entropy is maximum when the oscillation energy in each “atom” is the same, which coincides with the wavelet decomposition of stationary white noise. It is for this reason that an increase in entropy is considered a sign of a simplification of the structure of chaos.

This article uses wavelet-based entropy, which is transparently related to the entropy of the distribution of oscillation energy over a discrete set of frequency–time intervals. The value of this entropy depends on the choice of basis wavelet functions. This choice is made with the goal of finding a basis for which the maximum information is concentrated in the minimum wavelet coefficients. This choice corresponds to the minimum entropy. For this reason, entropy is called minimal.

In the future, we will be interested in the positions of the time points of a certain number of the largest local maxima or the smallest local minima of daily seismic noise properties in comparison with the times of earthquakes with a magnitude of at least 6 (Figure 3). To reduce the low-frequency components’ influence of changes in statistical values on the determination of the times of local extrema, the time series of noise properties were subjected to the operation of removing low frequencies using Gaussian kernel smoothing. Let  $u(t)$  be a time series with discrete time  $t$ . Gaussian kernel averaging of a time series  $u(t)$  with smoothing scale  $h > 0$  is defined by the formula [29]:

$$\bar{u}(t|h) = \sum_s u(s) \cdot \exp\left(-\left(\frac{t-s}{h}\right)^2\right) / \sum_s \exp\left(-\left(\frac{t-s}{h}\right)^2\right) \quad (1)$$

Next, the smoothed values for the scale  $h$  of 2 days were subtracted from the time series of statistical changes, and the most significant local extremum points were defined for the residuals. These operations are illustrated by the graphs in Figure 4(a2,b2,c2).

Extreme values exhibit the most pronounced effects of the noise statistics under consideration. While a key factor in seismic activity is its triggering nature, the occurrence of strong earthquakes is often attributed to small-scale factors, but the most likely result of such influence is precisely the extreme values.

The distribution of the most prominent local extremes of seismic noise properties is strongly influenced by the low-frequency components of their variations. To avoid their dominant influence, it is necessary to calculate the local extremes after suppressing the low frequencies. This is achieved by preliminary local smoothing of the noise property change time series and subsequent calculation of the residual from removing the local means. The radius of the Gaussian time window, equal to 2 days, was chosen as the minimum acceptable range.

Let us consider how the time points of the most significant local extrema of the statistics  $En$ ,  $\gamma$  and  $\Delta\alpha$  are distributed. To do this, we combine all the extremum points (352 smallest local minima  $\gamma$ ,  $\Delta\alpha$  and 352 largest local maxima of entropy  $En$ ) into a single time sequence, sort it in ascending order, and calculate the empirical probabilities of time values falling within successive six-month intervals; that is, we calculate a probability histogram of time points. Since the total length of observations is 29 years, the number of such intervals is 58. For all the statistics used, the last time interval in Figure 5 is characterized by a spike in

the empirical probability of extreme values. However, for the minimum values of the DJ index, this spike is the largest. It would have been possible to limit the analysis to the DJ index alone. However, this article uses a joint processing approach for three seismic noise statistics. Therefore, Figure 5 shows the result for this joint analysis. In the new version of the article, a separate probability histogram for the DJ index alone has been added to Figure 5. It shows that the last six-month interval has the highest empirical probability of containing local extremum points.

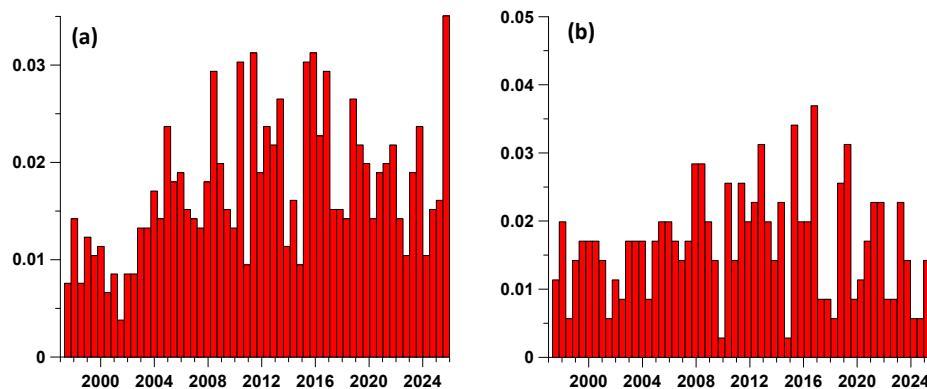


**Figure 5.** (a) Probability histogram of the time distribution of extreme values of three seismic noise properties (local maxima of  $En$  and local minima of  $\Delta\alpha \gamma$ ); (b) probability histogram for  $\gamma$  only. For each property, the number of most significant local extreme points is taken to be 352—the number of earthquakes with magnitudes of at least 6.

#### 4. Lead Times Between Local Extremes of Seismic Noise Properties and Earthquakes

To quantitatively estimate the relative positions of time points of local extrema of seismic noise properties and earthquake times, a measure of the mutual advance of point processes is used. This method was used in [30–34] to investigate the relationships between seismic noise properties, fluctuations of the global magnetic field, GPS tremor of the Earth’s surface, properties of the solar proton flux, and anomalies of meteorological parameters with the seismic process.

To conduct an analysis using the influence matrices method, the number of events in the two sequences being compared must be approximately equal. Choosing a minimum magnitude threshold of 6 ensures a sufficiently large number of events for the analysis to be statistically significant. On the other hand, magnitude 6 earthquakes are powerful enough for their preparation to be reflected in changes in seismic noise properties at a significant portion of the seismic network’s stations.

The lead measure is calculated using a parametric model of the intensity of two interacting point processes. Let  $t_j^{(\alpha)}$ ,  $j = 1, \dots, N_\alpha$ ;  $\alpha = 1, 2$  represent the time instants of two event streams. Let their intensities be represented as follows:

$$\lambda^{(\alpha)}(t) = c_0^{(\alpha)} + c_1^{(\alpha)} f^{(1)}(t) + c_2^{(\alpha)} f^{(2)}(t) \quad (2)$$

where  $c_0^{(\alpha)} \geq 0$ ,  $c_\beta^{(\alpha)} \geq 0$  are the parameters, and  $f^{(\beta)}(t)$  is the function of influence for events  $t_j^{(\beta)}$  of the flow with number  $\beta$ :

$$f^{(\beta)}(t) = \sum_{t_j^{(\beta)} < t} \exp(-(t - t_j^{(\beta)})/\tau) \quad (3)$$

From the Formula (3) it follows that the weight of the event with number  $j$  decays with relaxation time  $\tau$  for  $t > t_j^{(\beta)}$ . The parameter  $c_\beta^{(\alpha)}$  determines the degree of influence of the event stream  $\beta$  on the stream  $\alpha$ . The parameter  $c_\alpha^{(\alpha)}$  defines the strength of the stream  $\alpha$  on itself (self-excitation), and the parameter  $c_0^{(\alpha)}$  defines the stochastic component of intensity. For the fixed value of the parameter  $\tau$ , consider the problem of finding the parameters  $c_0^{(\alpha)}, c_\beta^{(\alpha)}$ .

The logarithmic likelihood function for a non-stationary Poisson process is equal to over the time interval  $[0, T]$  [35]:

$$\ln(L_\alpha) = \sum_{j=1}^{N_\alpha} \ln(\lambda^{(\alpha)}(t_j^{(\alpha)})) - \int_0^T \lambda^{(\alpha)}(s) ds, \quad \alpha = 1, 2 \quad (4)$$

It is necessary to find the maximum of functions (4) with respect to  $c_0^{(\alpha)}, c_\beta^{(\alpha)}$ . In [32,33] it was shown that problem (4) is reduced to the following:

$$\Phi^{(\alpha)}(c_1^{(\alpha)}, c_2^{(\alpha)}) = \sum_{j=1}^{N_\alpha} \ln(\lambda_0^{(\alpha)} + c_1^{(\alpha)} \Delta f^{(1)}(t_j^{(\alpha)}) + c_2^{(\alpha)} \Delta f^{(2)}(t_j^{(\alpha)})) \rightarrow \max_{c_1^{(\alpha)}, c_2^{(\alpha)}} \quad (5)$$

where  $\Delta f^{(\beta)}(t) = f^{(\beta)}(t) - \bar{f}^{(\beta)}$ ,  $\bar{f}^{(\beta)} = \int_0^T f^{(\beta)}(s) ds / T$ ,  $\lambda_0^{(\alpha)} = N_\alpha / T$ , under restrictions

$$c_1^{(\alpha)} \geq 0, c_2^{(\alpha)} \geq 0, c_1^{(\alpha)} \bar{f}^{(1)} + c_2^{(\alpha)} \bar{f}^{(2)} \leq \lambda_0^{(\alpha)} \quad (6)$$

Having solved problems (5) and (6) numerically, we can regard the elements of the influence matrix  $\kappa_\beta^{(\alpha)}$ ,  $\alpha = 1, 2$ ;  $\beta = 0, 1, 2$  by the following formulae:

$$\kappa_0^{(\alpha)} = c_0^{(\alpha)} / \lambda_0^{(\alpha)} \geq 0, \quad \kappa_\beta^{(\alpha)} = c_\beta^{(\alpha)} \cdot \bar{f}^{(\beta)} / \lambda_0^{(\alpha)} \geq 0 \quad (7)$$

The quantity  $\kappa_0^{(\alpha)}$  is the portion of the average intensity  $\lambda_0^{(\alpha)}$  of the process with index  $\alpha$ , which is purely random, the portion  $\kappa_\alpha^{(\alpha)}$  caused by self-excitation  $\alpha \rightarrow \alpha$ , and the portion  $\kappa_\beta^{(\alpha)}$ ,  $\beta \neq \alpha$  caused by external influence  $\beta \rightarrow \alpha$ . The influence matrix is defined by the following formula:

$$\begin{pmatrix} \kappa_0^{(1)} & \kappa_1^{(1)} & \kappa_2^{(1)} \\ \kappa_0^{(2)} & \kappa_1^{(2)} & \kappa_2^{(2)} \end{pmatrix} \quad (8)$$

The elements  $\kappa_0^{(1)}$  and  $\kappa_0^{(2)}$  present Poisson fractions of mean intensities. The elements  $\kappa_1^{(1)}$  and  $\kappa_2^{(2)}$  present self-excited components of mean intensity. The elements  $\kappa_2^{(1)}$  and  $\kappa_1^{(2)}$  defined the mutual excitation. For each row of the matrix (8) the sum equals 1. The matrices (8) are calculated in a moving time window of length  $L$  with mutual shift  $\Delta L$ .

Next, optimization is performed with respect to the parameters  $L, \tau$  with the aim of maximizing the average value of the difference  $\Delta\kappa = \kappa_2^{(1)} - \kappa_1^{(2)} \rightarrow \max_{\tau, L}$ , where  $\kappa_2^{(1)}$  is the portion of the intensity of the earthquake sequence (the first process) caused by the "influence" of the sequence of local extrema (the second process), and  $\kappa_1^{(2)}$  is the portion of the intensity of the sequence of local extrema caused by the leading influence of seismic events. We will agree to call  $\kappa_2^{(1)}$  the "direct" lead, and the  $\kappa_1^{(2)}$  "reverse" lead. The greater the difference  $\Delta\kappa$ , the greater the effect of the leading of the local extrema by the time instants relative to the time instants of the earthquakes. The problem of finding the maximum is solved within an a priori range of parameter variations:  $L_{\min} \leq L \leq L_{\max}$ ,  $\tau_{\min} \leq \tau \leq \tau_{\max}$ . The values  $L_{\min} = 0.5$ ,  $L_{\max} = 5$ ,  $\tau_{\min} = 0.05$ , and  $\tau_{\max} = 5$  were used in

the calculations; all time units are in years. The shift  $\Delta L$  of the time windows was taken equal to 0.05 years. Table 1 presents parameters of models (2) and (3) which were obtained after solving the problem  $\Delta\kappa \rightarrow \max_{\tau, L}$ .

**Table 1.** Values of optimal parameters of the intensity model of two related consecutive events for the extreme points of different properties of seismic noise and earthquake  $M \geq 6$  times.

| Property                  | $\gamma$ | $\Delta\alpha$ | $En$  |
|---------------------------|----------|----------------|-------|
| $\tau$ , years            | 0.055    | 0.080          | 0.052 |
| $L$ , years               | 0.93     | 2.58           | 1.91  |
| Mean of $\kappa_2^{(1)}$  | 0.315    | 0.399          | 0.410 |
| Mean of $\kappa_1^{(2)}$  | 0.129    | 0.145          | 0.186 |
| Difference $\Delta\kappa$ | 0.186    | 0.251          | 0.224 |

Figure 6 presents graphs of the values of  $\kappa_2^{(1)}$  and  $\kappa_1^{(2)}$  for points of local extrema of the analyzed properties of seismic noise with the optimal choice of parameters.

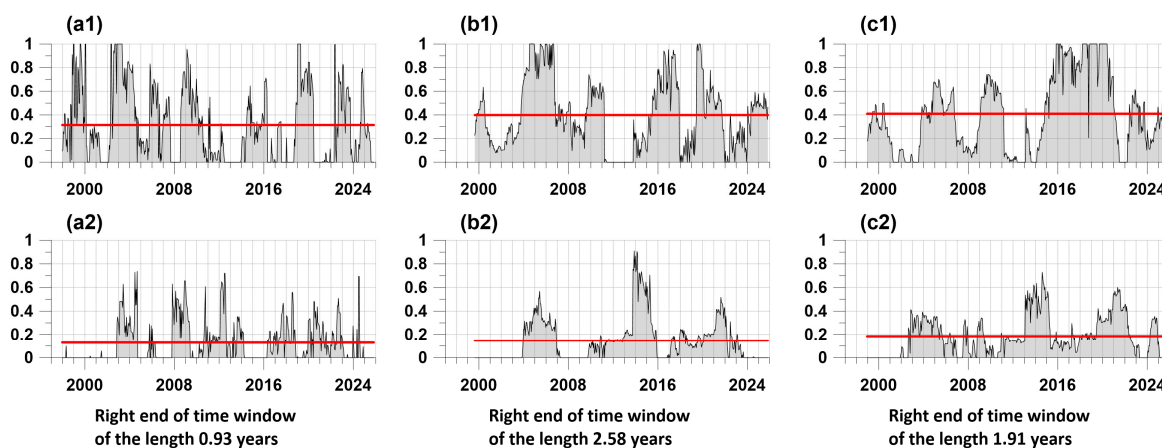


**Figure 6.** Figure (a1,b1,c1) presents graphs of the “direct” lead measures by the time points of the most pronounced local extrema of the values  $\gamma$ ,  $\Delta\alpha$  and  $En$  relative to the times of earthquakes with the optimal choice of the attenuation time  $\tau$  and the length  $L$  of the time window (Table 1). Figure (a2,b2,c2) presents graphs of the “inverse” lead measures by the time points of earthquakes  $M \geq 6$  relative to the time points of the most pronounced local extrema of the values  $\gamma$ ,  $\Delta\alpha$  and  $En$ . The horizontal red lines represent the average values of the “direct” and “inverse” lead measures (Table 1).

Let us denote by  $\bar{\kappa}_2^{(1)}$  the result of averaging the measures  $\kappa_2^{(1)}$  of “forward” advance for various properties of seismic noise, presented by the graphs in Figure 6(a1,b1,c1). This averaging is realized by calculating the Gaussian means of the union of these dependencies using Formula (1) for an averaging radius  $h$  equal to 10 days and for a uniform sequence of time points with a step of 10 days. Next, we calculate the same result  $\bar{\kappa}_1^{(2)}$  of averaging the measures  $\kappa_1^{(2)}$  of “reverse” advance, presented by the graphs in Figure 6(a2,b2,c2). Figure 7 shows their difference  $\Delta\bar{\kappa} = \bar{\kappa}_2^{(1)} - \bar{\kappa}_1^{(2)}$  in dependence on the position of the right end of successive time intervals of 10 days.

The median time interval between earthquakes with magnitudes  $M \geq 6$  in the region, presented Figure 1, equals 13.7 days. Therefore, a time step of 10 days was chosen as the closest “round” number.



**Figure 7.** Plot of the differences between the averaged forward and backward advance measures of the times of properties  $\gamma$ ,  $\Delta\alpha$  and  $En$  extremes relative to the times of earthquakes  $M \geq 6$ . The vertical blue line represents the time of the Tohoku mega-earthquake of 11 March 2011,  $M = 9.1$ . The horizontal red line represents the mean of the differences in the averaged advance measures, equal to 0.224. The two green lines represent the graphs of the best approximations by harmonic oscillations of the advance measure difference for time intervals before the Tohoku event (3.5-year period) and after 2015 (3.2-year period).

The value  $\Delta\bar{\kappa}$  is an integrated measure of the lead time of local extrema in seismic noise properties relative to the times of earthquakes with magnitudes of at least 6. The vertical blue line in Figure 7 represents the time of the Tohoku mega-earthquake of 11 March 2011. The graph in Figure 7 shows that this measure is mostly positive; that is, for most times, the points of local extrema in seismic noise statistics lead the times of earthquakes. An exception is a time interval of just under 4 years, adjacent to the time of the Tohoku event on the right and extending to the 2015 timestamp, when the value  $\Delta\bar{\kappa}$  is negative. The graph in Figure 7 also shows other time segments when  $\Delta\bar{\kappa} < 0$ , but they are not as long as after the Tohoku earthquake. The time intervals  $\Delta\bar{\kappa} < 0$  correspond to a situation when, on average, the attainment of extreme values of properties  $\gamma$ ,  $\Delta\alpha$  and  $En$  is a consequence of earthquakes. If  $\Delta\bar{\kappa} > 0$ , then this means that local extremes of noise properties foreshadow seismic events.

For two long time periods before the Tohoku event and after the 2015 timestamp, quasi-periodic fluctuations in the measure  $\Delta\bar{\kappa}$  values are noticeable. We estimate their periods by fitting harmonic oscillations (shown as green lines in Figure 7) using the least-squares method with unknown periods, which we find by minimizing the residual variance. It turns out that these periods are quite close to each other, equal to 3.5 years before the Tohoku event and 3.2 years after 2015.

## 5. The First Principal Components of the Amplitudes of the EEMD Envelope Decompositions of Seismic Noise Properties

Let us consider the issue of identifying the general fluctuations of the median values of the noise properties  $\gamma$ ,  $\Delta\alpha$  and  $En$ , the graphs of which are presented in Figure 4(a1,b1,c1). To solve this problem, we will use the Hilbert–Huang method [36,37] of decomposing signals into sequences of intrinsic mode functions (IMF), also known as empirical mode decomposition (EMD). The use of EMD has a wide range of applications. In [27], this method was used to analyze seismicity on various time scales in combination with multifractal analysis. In [31,33], EMD was used to analyze the prognostic properties of the earth’s surface of GPS-measured tremors and anomalies of meteorological time series.

The components of IMF decompositions can be formally associated with the frequency bands of the detail levels of wavelet decompositions or simply with the result of frequency bandpass Fourier filtering for a sequence of frequency bands with uniform frequencies on a logarithmic scale. The Hilbert–Huang decomposition differs from wavelet or Fourier decompositions in that it lacks a pre-assigned basis of orthogonal functions. This circum-

stance allows the Hilbert–Huang decomposition to take into account nonstationary and nonlinear effects much more flexibly [36,37].

The decomposition of an arbitrary signal  $x(t)$  into empirical modes is given by the following formula:

$$x(t) = \sum_{j=1}^n q_j(t) + \rho_n(t) \quad (9)$$

where  $q_j(t)$  is the  $j$ -th function,  $\rho_n(t)$  is the remainder, and  $n$  is the number of empirical modes.

Let us describe the iterations for determining empirical mode function for each level  $j$ . Let  $k$ ,  $k = 0, 1, \dots, K_j$  be the iteration index, where  $K_j$  is the final number of iterations. The iterations are described by the formula

$$q_j^{(k+1)}(t) = q_j^{(k)}(t) - \zeta_j^{(k)}(t) \quad (10)$$

Here,  $\zeta_j^{(k)}(t) = (A_j^{(k)}(t) + B_j^{(k)}(t))/2$ , where  $A_j^{(k)}(t)$  and  $B_j^{(k)}(t)$  are the upper and lower envelopes for the signal  $q_j^{(k)}(t)$ , which are constructed by 3rd-order splines over all local maxima and minima of the signal  $q_j^{(k)}(t)$ .

Iterations (10) are started with a zero step  $q_1^{(0)}(t) = x(t)$  for the first level. Next, the upper  $A_1^{(0)}(t)$  and lower  $B_1^{(0)}(t)$  envelopes are found, the mean line  $\zeta_1^{(0)}(t)$  is calculated, and  $q_1^{(1)}(t)$  is found using Formula (10). For  $q_1^{(1)}(t)$ , the upper  $A_1^{(1)}(t)$  and lower  $B_1^{(1)}(t)$  envelopes are determined, and the mean value  $\zeta_1^{(1)}(t)$  is found, and so on, up to the last iteration index  $K_1$ , after which the first empirical mode  $q_1(t)$  is considered to have been found.

Iterations are stopped according to the following condition:

$$\sum_t (q_j^{(k+1)}(t) - q_j^{(k)}(t))^2 / \sum_t (q_j^{(k)}(t))^2 \leq \Delta \quad (11)$$

where  $\Delta$  is a small number, for instance, 0.01. After the mode  $q_j(t)$  is found, the next mode  $q_{j+1}(t)$  is started to be found with iteration  $k = 0$ :

$$q_{j+1}^{(0)}(t) = x(t) - q_j(t) \quad (12)$$

A new signal for subsequent decomposition is defined by subtraction (12) of the high-frequency component from the original signal. The construction of empirical oscillation modes continues until the number of local extrema becomes too small to be used to construct envelopes.

As the empirical mode level number  $j$  increases, the signals  $q_j(t)$  become increasingly low-frequency and tend toward an unchanging form. The sequence  $q_1(t), q_2(t), \dots, q_n(t)$  is constructed so that its sum gives an approximation (9) of the original signal.

Empirical oscillation modes, known as intrinsic mode functions (IMFs), are orthogonal to each other, thus forming the empirical basis for decomposing the original signal. From here on, these decomposition levels will be referred to as IMF levels.

One of the drawbacks of the EMD method is an “intermittency” which occurs when a single empirical mode includes signals of different scales. To overcome this effect of mode mixing, in [37] the Ensemble Empirical Mode Decomposition (EEMD) method was proposed. The EEMD modification could be presented as the following steps.

1. Adding a white noise realization to the original data.
2. EMD decomposing into empirical modes with the added white noise.

3. Repeating steps 1 and 2 a sufficiently large number of times with independent white noise realizations.

4. Obtaining the ensemble mean for the corresponding empirical modes.

The sequence of artificial observations is simulated in real time series:

$$x^{(i)}(t) = x(t) + \varepsilon_i(t) \quad (13)$$

where  $\varepsilon_i(t)$  is the  $i$ -th realization of white noise. In our calculations, we used 1000 realizations of independent white noise with a standard deviation equal to 0.1 of the standard deviation of the original signals.

After obtaining EEMD realizations of daily time series of noise properties  $\gamma$ ,  $\Delta\alpha$  and  $En$  for a sequence of IMF levels, we calculate the amplitudes of their envelopes using the Hilbert transform, which is efficiently implemented using the fast Fourier transform [38]. For each IMF level, we have three time functions of the envelope amplitudes corresponding to different properties of seismic noise. To isolate their common properties at each level, we calculate their first principal component after centering and normalization to unit variance [39,40]. The graphs of the first principal components of the envelope amplitudes are presented in Figure 8 for the first eight IMF levels of the EEMD. Each IMF level approximately corresponds to a frequency band with boundary periods from  $2^j\Delta t$  to  $2^{(j+1)}\Delta t$ , where  $j$  is the IMF level number and  $\Delta t$  is the time sampling step (in our case, 1 day).

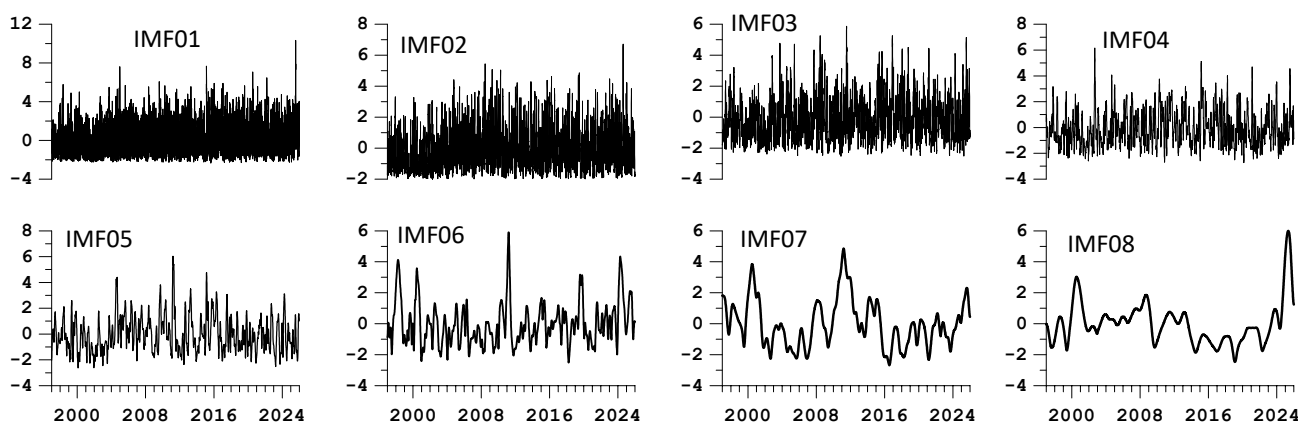


**Figure 8.** Graphs of the first principal components of the amplitudes of the envelopes of the daily median values of the properties  $\gamma$ ,  $\Delta\alpha$  and  $En$ , calculated for the EEMD realizations at the first eight IMF levels of the expansion into empirical oscillation modes.

Among the graphs in Figure 8, the low-frequency IMF levels 5–8 are particularly striking. At IMF levels 5–7, peaks in the first principal component centered on the time of the Tohoku mega-earthquake of 11 March 2011, are visible, indicating a post-seismic response. However, the IMF level 8 graph (periods from 256 to 512 days) displays a significant peak for the time interval from mid-2024 to late 2025, which may indicate preparation for the next strong earthquake.

The greatest synchronization of the envelope amplitudes at the 8th IMF level (the lowest frequency) in 2025 may indicate that a very powerful earthquake is preparing in the Pacific Trench near the coast of Japan, which may reach magnitude 10, as follows from the estimates in the article [8]. As for the bursts of the first principal component of the envelopes at the IMF06–IMF08 levels around 2002, they may foreshadow the earthquake of 25 September 2003, off the coast of Hokkaido with a magnitude of 8.3.

## 6. Extreme Values Probability Densities

Let us study the variability of the spatial distribution of extreme values of seismic noise properties. For this purpose, we consider a regular grid of  $30 \times 30$  nodes, covering an area with latitude from  $28^\circ$  N to  $46^\circ$  N and longitude from  $128^\circ$  E to  $146^\circ$  E (Figure 1). Let  $W$  be any value of  $\gamma$ ,  $\Delta\alpha$  or  $En$ . For each grid node  $(i, j)$  and for each day with number  $t$ , we find the five nearest working seismic stations, which yields five values of  $W$ . Let us denote by  $W_{ij}^{(t)}$  the median value of these five properties at a node  $(i, j)$  on a day with number  $t$ . The values  $W_{ij}^{(t)}$  in the set of nodes of the regular grid can be considered as an elementary daily map. For each daily map with a discrete time index  $t$  let us find the coordinates of the nodes  $\zeta_{mn}^{(t)} = (x_m^{(t)}, y_n^{(t)})$  at which a given number  $n_m$  of extreme values of  $W$  is reached relative to all other nodes of the regular grid. Minima are found for  $W = \Delta\alpha$  or  $W = \gamma$ , and maxima are found for  $W = En$ . Further,  $n_m = 10$  extreme values will be used. The set of two-dimensional vectors  $\zeta_{mn}^{(t)}$  considered within the time interval  $t \in [t_0, t_1]$  forms a random set. We estimate the two-dimensional probability distribution function of the vectors  $\zeta_{mn}^{(t)}$  for each node of the regular grid. For each node  $(i, j)$ , the probability density function of the distribution of extreme values of the property  $W$  is calculated according to the Parzen–Rosenblatt estimate with the Gaussian kernel function [40]:

$$p(\zeta_{ij}|t_0, t_1) = \frac{1}{2\pi n_m H^2 N_{t_0, t_1}} \sum_{t=t_0}^{t_1} \sum_{mn} \exp\left(-\frac{|\zeta_{ij} - \zeta_{mn}^{(t)}|^2}{2H^2}\right) \quad (14)$$

Here,  $H$  is the kernel averaging scale,  $t_0, t_1$  are integer indices that number the daily elementary maps, and  $N_{t_0, t_1} = (t_1 - t_0 + 1)$  is the daily maps number within the time interval under consideration. A smoothing scale  $H = 1^\circ$  was used.

Let us calculate the two-dimensional distribution densities (14) of extreme values in successive time windows of 10 days in length ( $N_{t_0, t_1} = 10$ ). Since we have three such distributions, we will calculate their weighted average. The weights are the squared values of the main eigenvector (corresponding to the maximum eigenvalue) components of the correlation matrix of probability densities [39]. By construction, the sum of weights equals to 1. Figure 9 shows graphs of the weighting coefficients depending on the position of the right end of time windows of 10 days in length.

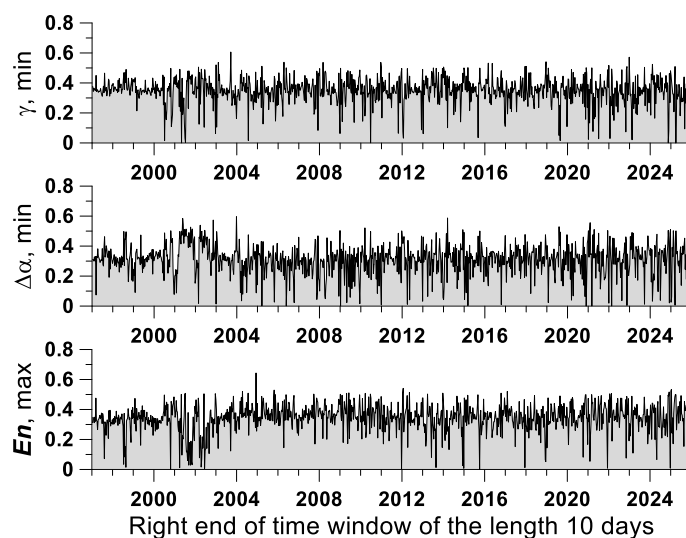


**Figure 9.** Graphs of changes in the weights of the probability densities of extreme values of properties  $\gamma$ ,  $\Delta\alpha$  (minima) and  $En$  (maxima) in successive time windows of 10 days in length.

To quantitatively describe the sequence of values of the weighted probability density function (PDF) for the distribution of extreme seismic noise properties in 10-day time windows, we consider the entropy of these densities. Let  $M$  be the number of grid nodes within the region formed by the union of circles with a radius of 250 km, centered at each F-net station (Figure 1). We calculate the histogram of the weighted probability density functions for each 10-day interval  $j$  as a sequence of values:

$$h_k^{(j)} = m_k^{(j)} / M_b, \quad k = 1, \dots, M_b \quad (15)$$

where  $M_b$  is the number of intervals dividing the range of density variation within a given 10-day window into intervals of equal length. According to recommendations [29,40], we choose the value  $M_b = \sqrt{M}$ . Obviously  $\sum_k h_k^{(j)} = 1$ , the values of the histogram (15) also have the properties of a discrete probability distribution. We define the normalized entropy of this distribution by the following formula:

$$Q_j = - \sum_{k=1}^{M_b} h_k^{(j)} \log(h_k^{(j)}) / \log(M_b), \quad 0 \leq Q_j \leq 1 \quad (16)$$

In Figure 10, the gray line represents the graph of entropy change (16) depending on the position of the right end of 10-day time windows. The red line represents the result of smoothing with a Gaussian kernel (Formula (1)) with a smoothing kernel width  $h$  of 400 days.

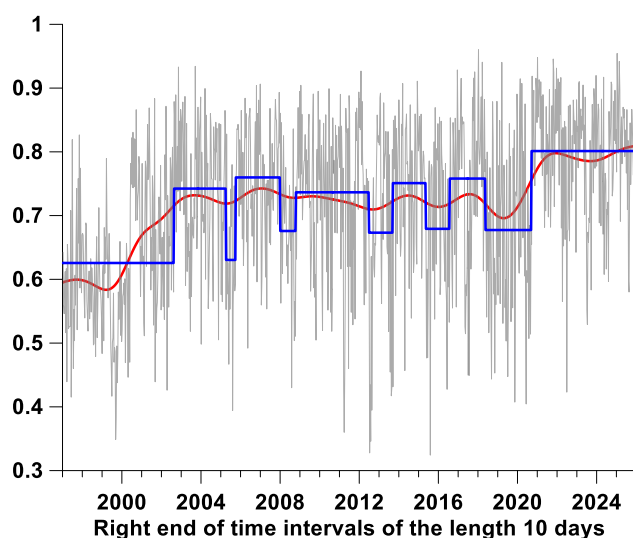


**Figure 10.** The gray line represents the change in the entropy of the weighted probability density function of extreme values of properties  $\gamma$ ,  $\Delta\alpha$  and  $En$ , calculated in successive 10-day time windows. The blue line represents the stepwise WTMM approximation, which divides the time interval into 12 segments with different mean entropy values. The red line represents the smoothed entropy values with a Gaussian window of radius 400 days.

The blue line represents a stepwise approximation using so-called long WTMM (Wavelet Transform Modulus Maxima) chains of the signal skeleton. Scale-dependent stepwise approximation allows one to formally determine the moments in time of significant changes in the mean entropy values. This approximation is constructed using continuous wavelet transforms with a kernel in the form of derivatives of a Gaussian function, which allows one to formalize the selection of moments in time at which a significant, scale-dependent change in the mean value of a noisy signal occurs [11,41].

To describe the construction of the stepwise WTMM approximation, we will use continuous-time formulas, which are easily adapted to the discrete-time case but are more compact. The smoothed entropy value is calculated using the following formula:

$$Q_0(t, a) = \frac{\int_{-\infty}^{+\infty} Q(t + av) \cdot \psi_0(v) dv}{\int_{-\infty}^{+\infty} \psi_0(v) dv}, \quad \psi_0(v) = \exp(-v^2) \quad (17)$$

where  $a > 0$  is the smoothing time scale. For the  $n$ -th derivative of the smoothed signal, divided by  $n!$  (the Taylor coefficient), the following expression holds:

$$Q_n(t, a) \equiv \frac{1}{n!} \frac{d^n Q_0(t, a)}{dt^n} = \frac{\int_{-\infty}^{+\infty} Q(t + av) \psi_n(v) dv}{a^n \int_{-\infty}^{+\infty} v^n \psi_n(v) dv} \quad (18)$$

where  $\psi_n(v) = (-1)^n \cdot \frac{d^n \psi_0(v)}{dv^n} \equiv (-1)^n \cdot \psi_0^{(n)}(v)$ . A two-dimensional WTMM point  $(t, a)$  for  $n \geq 0$  is defined as a point for which  $|Q_n(t, a)|$  exhibits a local maximum in time  $t$  for a given time scale  $a$ . For  $n = 0$ , WTMM points are present points of local extrema (maxima or minima) of the smoothed signal  $Q_0(t, a)$ , which can be combined into chains. The set of all chains forms the WTMM skeleton of the signal. If the kernel  $\psi_0(v)$  is Gaussian, then a given chain of the WTMM skeleton does not terminate (does not “hang in the air”) when decreasing the scale and touches the time axis [42]. The WTMM points for the 1st-order derivative  $Q_1(t, a)$  indicate the time points of maximum trend (positive or negative) of the smoothed signal  $Q_0(t, a)$  for a given scale  $a$ . This can be used to formally identify points of large changes in the mean. These times correspond to the roots of long WTMM chains reaching given values of the scale  $a^*$ . We define a stepwise WTMM approximation for a signal  $Q(t)$  as a function that is equal to a sequence of constant values  $\bar{Q}_k$  in intervals  $[\tau_k(a^*), \tau_{k+1}(a^*)]$ . Here,  $\tau_k(a^*)$  denotes the beginnings of WTMM chains for  $Q_1(t, a)$ , which exceeds a threshold time scale  $a^*$ , and stepwise approximation equals the sequence of average values  $\bar{Q}_k$  within the time intervals  $[\tau_k(a^*), \tau_{k+1}(a^*)]$ .

In Figure 10, the blue line represents the stepwise WTMM approximation for the parameter  $a^* = 450$  days. This threshold time scale ensures that the overall time interval is divided into 12 fragments with different average entropy values, which are then interpreted as stages in the development of seismic noise field features in the Japanese islands. A comparison of the red and blue lines in Figure 10 shows that both averaging methods exhibit roughly the same behavior in the most general trends. In particular, the final time interval from the end of 2020 is characterized by elevated average entropy values.

## 7. A Sequence of Distribution Maps of Average-Weighted Probability Densities of Extreme Values of Noise Properties

Figure 11 shows a sequence of distributions of average-weighted probability densities of extreme values of seismic noise properties for 12 time intervals allocated by the stepwise WTMM approximation of entropy (16).

Within the framework of the considered hypothesis, the areas of concentration of the weighted probability density are interpreted as “spots of increased seismic hazard.” The time intervals identified by the stepwise approximation of entropy (16) can be represented as a sequence of 12 stages of precursor development based on the properties of seismic noise. The first six distribution maps ( $\alpha 01$ – $\alpha 06$ ) correspond to the time intervals preceding the Tohoku event, the epicenter of which is shown by a black asterisk. In the first two maps ( $\alpha 01, \alpha 02$ ), it is noticeable how a single area of concentration of the probability density at  $\alpha 01$  splits into two parts, one of which at  $\alpha 02$  closely approaches the epicenter of the Tohoku event. Stage  $\alpha 03$  lasts for approximately six months, and during this short period

of time, for which the average entropy value (16) declines, a region of probability density concentration formed in the region of  $30^{\circ} \text{ N} \leq \text{Lat} \leq 34^{\circ} \text{ N}$ ,  $136^{\circ} \text{ E} \leq \text{Lon} \leq 140^{\circ} \text{ E}$ , which remains stable for all later stages. A clear precursor to the future Tohoku mega-earthquake of 11 March 2011 formed during stages ( $\alpha 04$ – $\alpha 06$ ). Note the significant duration of the time interval corresponding to stage  $\alpha 06$ .

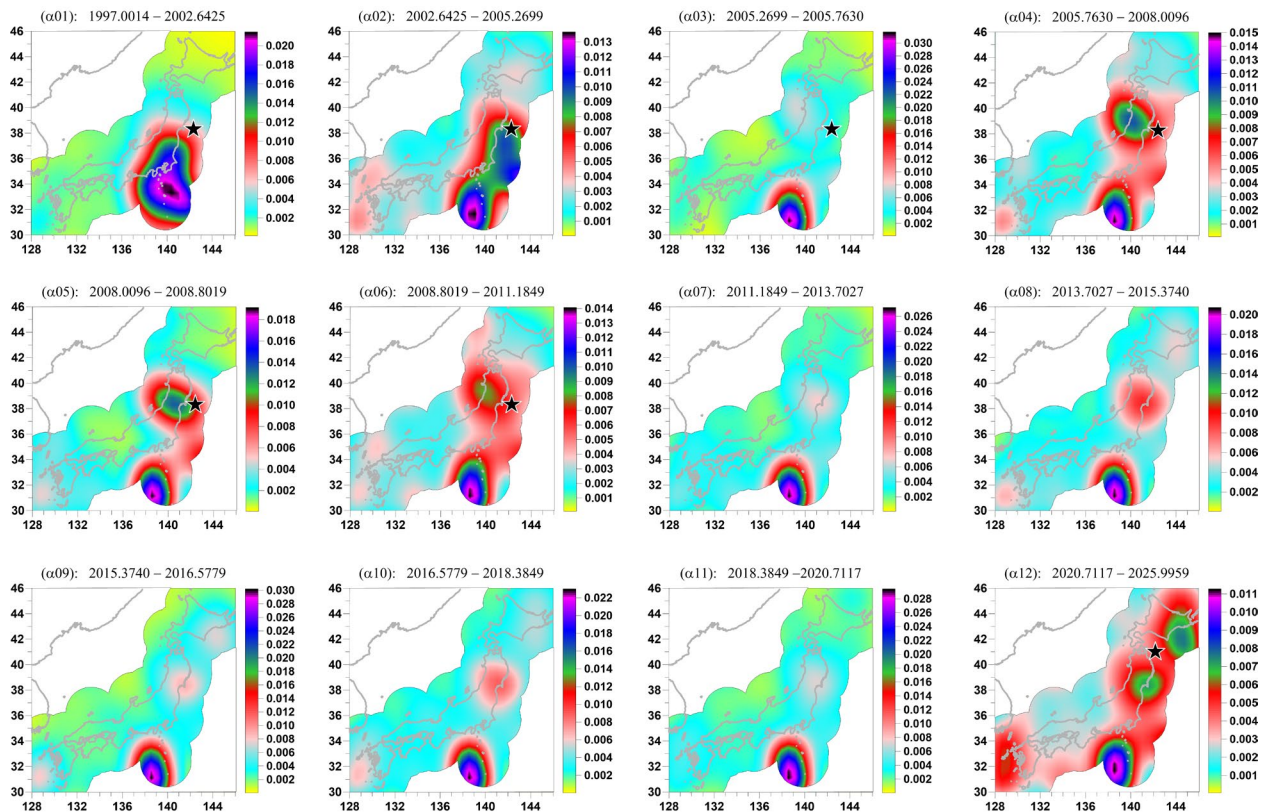


**Figure 11.** The two-dimensional weighted average probability densities for extreme values of the properties  $\gamma$ ,  $\Delta\alpha$  and  $En$ , averaged over 12 time intervals identified using the stepwise WTMM approximation of entropy, are presented. The time boundaries of the intervals are indicated at the top of each two-dimensional distribution map as fractional years. In the maps ( $\alpha 01$ – $\alpha 06$ ) for six time intervals before the Tohoku earthquake of 11 March 2011,  $M = 9.1$ , the position of the hypocenter of this event is shown by a black asterisk. In the map ( $\alpha 12$ ), the position of the hypocenter of the Aomori earthquake of 8 December 2025,  $M = 7.6$ , is shown by a black asterisk.

Five stages ( $\alpha 07$ – $\alpha 11$ ) demonstrate a relatively calm evolution of “seismic hazard spots” with periodic moderate concentration of probability density in the Tohoku aftershock region, the bursts of which correspond to an increase in the average entropy values (16) in Figure 10. Finally, the last stage,  $\alpha 12$ , is characterized by a significant rearrangement of the configuration of seismic hazard spots. Concentration of probability density is observed along the entire length of the Pacific coast of Japan (subduction region), while the area of the highest density values remains low-lying in the region  $30^{\circ} \text{ N} \leq \text{Lat} \leq 34^{\circ} \text{ N}$ ,  $136^{\circ} \text{ E} \leq \text{Lon} \leq 140^{\circ} \text{ E}$ . During stage  $\alpha 12$ , the Aomori earthquake occurred on 8 December 2025,  $M = 7.6$ , the epicenter of which is shown by a black asterisk on the  $\alpha 12$  map.

The region  $30^{\circ} \text{ N} \leq \text{Lat} \leq 34^{\circ} \text{ N}$ ,  $136^{\circ} \text{ E} \leq \text{Lon} \leq 140^{\circ} \text{ E}$  finally formed at stage  $\alpha 03$  and remains a stable region of elevated seismic hazard for all subsequent stages. At stages  $\alpha 04$ – $\alpha 06$ , a region of elevated seismic hazard is visible in the region of the 11 March 2011 Tohoku mega-earthquake, which is interpreted as a precursor. This region disappears completely at stage  $\alpha 07$  after the mega-earthquake, but at stages  $\alpha 08$ – $\alpha 11$ , it manifests as episodic activation of moderate seismic hazard in the aftershock region of the Tohoku event.

As for the final stage of  $\alpha_{12}$ , the seismic hazard zone encompasses the entire Pacific coast of Japan, but the region  $30^\circ \text{ N} \leq \text{Lat} \leq 34^\circ \text{ N}$ ,  $136^\circ \text{ E} \leq \text{Lon} \leq 140^\circ \text{ E}$  remains dominant. Therefore, it is interpreted as the most likely location for the next mega-earthquake.

## 8. Conclusions

A method for analyzing the evolution of low-frequency seismic noise field properties in a seismically active region is proposed. This method is based on studying the temporal and spatial distribution of extreme values of noise properties, which describe the complexity of its statistical structure. An increase in seismic hazard is interpreted as a simplification of the noise structure and its approach to the properties of white noise, as well as the synchronization of temporal variations in these properties. A method for identifying stages in the development of a seismic noise field is proposed based on a stepwise WTMM approximation of the change in the entropy of the distribution of weighted average densities of the distribution of extreme values of seismic noise properties. The method is applied to the analysis of noise properties on the Japanese islands over 29 years of observations, 1997–2025.

The main conclusions are that the spatial and temporal behavior of low-frequency seismic noise properties in Japan since 2020, and particularly in the last two years, reveal a number of indicators that point to the preparation of the next strong earthquake. Figure 5 shows a spike in the probability histogram of the distribution of time points when the values of the properties under consideration reach extreme values over the last six months. Figure 7 shows a pattern of quasi-periodic oscillations in the average integrated measure of the lead time of seismic noise property extreme points relative to the time points of strong earthquakes with a magnitude of at least 6 since 2015, with a peak value at the end of 2025, following a four-year interval when this pattern disappeared following the Tohoku mega-earthquake of 11 March 2011. Figure 8 shows a spike in the first principal component of the envelope amplitudes for the EEMD Hilbert–Huang decomposition of the daily median values of three seismic noise properties for the lowest-frequency IMF level number 8 (characteristic periods from 256 to 512 days) for the 2024–2025 time interval. This spike indicates synchronization of low-frequency variations in seismic noise properties. Figure 10 shows that the average entropy values of the weighted average probability density distribution of noise property extremes reach their maximum values from the end of 2020 to the end of 2025. Figure 11, which visualizes 12 stages of seismic noise field development on the Japanese islands, shows that the situation before the Tohoku mega-earthquake (stages ( $\alpha_{04}$ – $\alpha_{06}$ )) is repeated at the final stage,  $\alpha_{12}$ , in that new “seismic hazard” spots appear, covering the entire Pacific coast of Japan. At the same time, the maximum probability density in the southern part of the studied area of the Japanese islands, which formed at stage  $\alpha_{03}$ , remains stable.

Taken together, these features are interpreted as indicators of increased current seismic hazard, with particular attention to the region  $30^\circ \text{ N} \leq \text{Lat} \leq 34^\circ \text{ N}$ ,  $136^\circ \text{ E} \leq \text{Lon} \leq 140^\circ \text{ E}$ . Naturally, this is not a prediction of the timing of the next strong earthquake; the essence of this study is to detect a trend of increasing seismic hazard.

**Funding:** This research received no external funding.

**Data Availability Statement:** The original seismic data are contained in the database at <http://www.fnet.bosai.go.jp/faq/?LANG=en> (accessed on 4 January 2026). Information about seismic processes was taken from <https://earthquake.usgs.gov/earthquakes/search> (accessed on 4 January 2026).

**Acknowledgments:** This work was carried out within the framework of the state assignments of the Institute of Physics of the Earth of the Russian Academy of Sciences.

**Conflicts of Interest:** The author declares that the research was conducted in the absence of any commercial or financial relationships that could be construed as potential conflicts of interest.

## References

- Lyubushin, A. Synchronization of Geophysical Fields Fluctuations. In *Complexity of Seismic Time Series: Measurement and Applications*; Chelidze, T., Telesca, L., Vallianatos, F., Eds.; Elsevier: Amsterdam, The Netherlands; Oxford, UK; Cambridge, UK, 2018; Chapter 6, pp. 161–197. [[CrossRef](#)]
- Lyubushin, A.A. Seismic Noise Wavelet-Based Entropy in Southern California. *J. Seismol.* **2020**, *25*, 25–39. [[CrossRef](#)]
- Lyubushin, A. Low-Frequency Seismic Noise Properties in the Japanese Islands. *Entropy* **2021**, *23*, 474. [[CrossRef](#)] [[PubMed](#)]
- Rikitake, T. Probability of a great earthquake to recur in the Tokai district, Japan: Reevaluation based on newly-developed paleoseismology, plate tectonics, tsunami study, micro-seismicity and geodetic measurements. *Earth Planets Space* **1999**, *51*, 147–157. [[CrossRef](#)]
- Mogi, K. Two grave issues concerning the expected Tokai Earthquake. *Earth Planets Space* **2004**, *56*, li–lxvi. [[CrossRef](#)]
- Simons, M.; Minson, S.E.; Sladen, A.; Ortega, F.; Jiang, J.; Owen, S.E.; Meng, L.; Ampuero, J.-P.; Wei, S.; Chu, R.; et al. The 2011 Magnitude 9.0 Tohoku-Oki earthquake: Mosaicking the megathrust from seconds to centuries. *Science* **2011**, *332*, 911. [[CrossRef](#)]
- Kagan, Y.Y.; Jackson, D.D. Tohoku Earthquake: A Surprise? *Bull. Seismol. Soc. Am.* **2013**, *103*, 1181–1194. [[CrossRef](#)]
- Zoller, G.; Holschneider, M.; Hainzl, S.; Zhuang, J. The largest expected earthquake magnitudes in Japan: The statistical perspective. *Bull. Seismol. Soc. Am.* **2014**, *104*, 769–779. [[CrossRef](#)]
- Broadband Seismograph Network NIED F-Net. Available online: <http://www.fnet.bosai.go.jp/faq/?LANG=en> (accessed on 4 January 2026).
- USGS Search Earthquake Catalog. Available online: <https://earthquake.usgs.gov/earthquakes/search/> (accessed on 4 January 2026).
- Mallat, S.A. *Wavelet Tour of Signal Processing*, 2nd ed.; Academic Press: San Diego, CA, USA; London, UK; Boston, MA, USA; New York, NY, USA; Sydney, Australia; Tokyo, Japan; Toronto, ON, Canada, 1999.
- Donoho, D.L.; Johnstone, I.M. Adapting to unknown smoothness via wavelet shrinkage. *J. Am. Stat. Assoc.* **1995**, *90*, 1200–1224. [[CrossRef](#)]
- Taqqu, M.S. Self-similar processes. In *Encyclopedia of Statistical Sciences*; Wiley: New York, NY, USA, 1988; Volume 8, pp. 352–357.
- Feder, J. *Fractals*; Plenum Press: New York, NY, USA; London, UK, 1988.
- Kantelhardt, J.W.; Zschiegner, S.A.; Konsciency-Bunde, E.; Havlin, S.; Bunde, A.; Stanley, H.E. Multifractal detrended fluctuation analysis of nonstationary time series. *Physica A* **2002**, *316*, 87–114. [[CrossRef](#)]
- Costa, M.; Peng, C.-K.; Goldberger, A.L.; Hausdorff, J.M. Multiscale entropy analysis of human gait dynamics. *Physica A* **2003**, *330*, 53–60. [[CrossRef](#)]
- Costa, M.; Goldberger, A.L.; Peng, C.-K. Multiscale entropy analysis of biological signals. *Phys. Rev. E* **2005**, *71*, 021906. [[CrossRef](#)] [[PubMed](#)]
- Varotsos, P.A.; Sarlis, N.V.; Skordas, E.S.; Lazaridou, M.S. Entropy in the natural time domain. *Phys. Rev. E* **2004**, *70*, 011106. [[CrossRef](#)] [[PubMed](#)]
- Varotsos, P.A.; Sarlis, N.V.; Skordas, E.S. *Natural Time Analysis: The New View of Time*; Precursory Seismic Electric Signals, Earthquakes and other Complex Time Series; Springer: Berlin/Heidelberg, Germany, 2011. [[CrossRef](#)]
- Koutaloni, I.; Vallianatos, F. Evidence of Non-extensivity in Earth's Ambient Noise. *Pure Appl. Geophys.* **2017**, *174*, 4369–4378. [[CrossRef](#)]
- Vallianatos, F.; Koutaloni, I.; Chatzopoulos, G. Evidence of Tsallis entropy signature on medicane induced ambient seismic signals. *Physica A* **2019**, *520*, 35–43. [[CrossRef](#)]
- Ivanov, P.C.; Amaral, L.A.N.; Goldberger, A.L.; Havlin, S.; Rosenblum, M.B.; Struzik, Z.; Stanley, H.E. Multifractality in healthy heartbeat dynamics. *Nature* **1999**, *399*, 461–465. [[CrossRef](#)]
- Humeau, A.; Chapeau-Blondeau, F.; Rousseau, D.; Rousseau, P.; Trzepizur, W.; Abraham, P. Multifractality, sample entropy, and wavelet analyses for age-related changes in the peripheral cardiovascular system: Preliminary results. *Med. Phys. Am. Assoc. Phys. Med.* **2008**, *35*, 717–727. [[CrossRef](#)]
- Dutta, S.; Ghosh, D.; Chatterjee, S. Multifractal detrended fluctuation analysis of human gait diseases. *Front. Physiol.* **2013**, *4*, 274. [[CrossRef](#)]
- Telesca, L.; Colangelo, G.; Lapenna, V. Multifractal variability in geoelectrical signals and correlations with seismicity: A study case in southern Italy. *Nat. Hazards Earth Syst. Sci.* **2005**, *5*, 673–677. [[CrossRef](#)]
- Telesca, L.; Lovallo, M. Analysis of the time dynamics in wind records by means of multifractal detrended fluctuation analysis and the Fisher-Shannon information plane. *J. Stat. Mech.* **2011**, *2011*, P07001. [[CrossRef](#)]
- Sarlis, N.V.; Skordas, E.S.; Mintzels, A.; Papadopoulou, K.A. Micro-scale, mid-scale, and macro-scale in global seismicity identified by empirical mode decomposition and their multifractal characteristics. *Sci. Rep.* **2018**, *8*, 9206. [[CrossRef](#)]
- Mintzels, A.; Sarlis, N.V.; Christopoulos, S.-R.G. Estimation of multifractality based on natural time analysis. *Physica A* **2018**, *512*, 153–164. [[CrossRef](#)]

29. Hardle, W. *Applied Nonparametric Regression*; Biometric Society Monographs No. 19; Cambridge University Press: Cambridge, UK, 1990.
30. Lyubushin, A.; Rodionov, E. Wavelet-based correlations of the global magnetic field in connection to strongest earthquakes. *Adv. Space Res.* **2024**, *74*, 3496–3510. [[CrossRef](#)]
31. Lyubushin, A.; Rodionov, E. Prognostic Properties of Instantaneous Amplitudes Maxima of Earth Surface Tremor. *Entropy* **2024**, *26*, 710. [[CrossRef](#)] [[PubMed](#)]
32. Lyubushin, A.; Rodionov, E. Quantitative Assessment of the Trigger Effect of Proton Flux on Seismicity. *Entropy* **2025**, *27*, 505. [[CrossRef](#)] [[PubMed](#)]
33. Lyubushin, A.; Kopylova, G.; Rodionov, E.; Serafimova, Y. An Analysis of Meteorological Anomalies in Kamchatka in Connection with the Seismic Process. *Atmosphere* **2025**, *16*, 78. [[CrossRef](#)]
34. Lyubushin, A.; Rodionov, E. The Relationship Between the Seismic Regime and Low-Frequency Variations in Meteorological Parameters Measured at a Network of Stations in Japan. *Atmosphere* **2025**, *16*, 1129. [[CrossRef](#)]
35. Cox, D.R.; Lewis, P.A.W. *The Statistical Analysis of Series of Events*; Methuen: London, UK, 1996.
36. Huang, N.E.; Shen, Z.; Long, S.R.; Wu, V.C.; Shih, H.H.; Zheng, Q.; Yen, N.C.; Tung, C.C.; Liv, H.H. The empirical mode decomposition and the Hilbert spectrum for nonlinear and non-stationary time series analysis. *Proc. Roy. Soc. Lond. Ser. A* **1998**, *454*, 903–995. [[CrossRef](#)]
37. Huang, N.E.; Wu, Z. A review on Hilbert-Huang transform: Method and its applications to geophysical studies. *Rev. Geophys.* **2008**, *46*, RG2006. [[CrossRef](#)]
38. Bendat, J.S.; Piersol, A.G. *Random Data. Analysis and Measurement Procedures*, 4th ed.; Wiley & Sons: Hoboken, NJ, USA, 2010.
39. Jolliffe, I.T. *Principal Component Analysis*; Springer: Berlin/Heidelberg, Germany, 1986. [[CrossRef](#)]
40. Duda, R.O.; Hart, P.E.; Stork, D.G. *Pattern Classification*; Wiley-Interscience Publication: New York, NY, USA; Chichester, UK; Brisbane, Australia; Singapore; Toronto, ON, Canada, 2000.
41. Mallat, S.; Zhong, S. Characterization of signals from multiscale edges. *IEEE Trans. Pattern Anal. Mach. Intell.* **1992**, *14*, 710–732. [[CrossRef](#)]
42. Hummel, B.; Moniot, R. Reconstruction from zero-crossings in scale-space. *IEEE Trans. Acoust. Speech Signal Process.* **1989**, *37*, 2111–2130. [[CrossRef](#)]

**Disclaimer/Publisher’s Note:** The statements, opinions and data contained in all publications are solely those of the individual author(s) and contributor(s) and not of MDPI and/or the editor(s). MDPI and/or the editor(s) disclaim responsibility for any injury to people or property resulting from any ideas, methods, instructions or products referred to in the content.